



# **A robust inverse analysis method for elastoplastic behavior identification using the true geometry modeling of Berkovich indenter**

César Moisés Sánchez-Camargo, Anis Hor, Catherine Mabru

## **► To cite this version:**

César Moisés Sánchez-Camargo, Anis Hor, Catherine Mabru. A robust inverse analysis method for elastoplastic behavior identification using the true geometry modeling of Berkovich indenter. International Journal of Mechanical Sciences, 2020, 171, pp.105370. <10.1016/j.ijmecsci.2019.105370>. <hal-03036472>

**HAL Id: hal-03036472**

**<https://hal.science/hal-03036472v1>**

Submitted on 2 Dec 2020

**HAL** is a multi-disciplinary open access archive for the deposit and dissemination of scientific research documents, whether they are published or not. The documents may come from teaching and research institutions in France or abroad, or from public or private research centers.

L'archive ouverte pluridisciplinaire **HAL**, est destinée au dépôt et à la diffusion de documents scientifiques de niveau recherche, publiés ou non, émanant des établissements d'enseignement et de recherche français ou étrangers, des laboratoires publics ou privés.



HAL Authorization



## Open Archive Toulouse Archive Ouverte (OATAO)

OATAO is an open access repository that collects the work of some Toulouse researchers and makes it freely available over the web where possible.

This is an author's version published in: <https://oatao.univ-toulouse.fr/26942>

**Official URL :** <https://doi.org/10.1016/j.ijmecsci.2019.105370>

### To cite this version :

Sánchez Camargo, César Moisés and Hor, Anis and Mabru, Catherine A robust inverse analysis method for elastoplastic behavior identification using the true geometry modeling of Berkovich indenter. (2020) International Journal of Mechanical Sciences, 171. 105370. ISSN 0020-7403

Any correspondence concerning this service should be sent to the repository administrator:

[tech-oatao@listes-diff.inp-toulouse.fr](mailto:tech-oatao@listes-diff.inp-toulouse.fr)

# A robust inverse analysis method for elastoplastic behavior identification using the true geometry modeling of Berkovich indenter

Cesar-Moises Sanchez-Camargo\*, Anis Hor, Catherine Mabru

Institut Clément Ader (ICA), Université de Toulouse, CNRS, ISAE-SUPAERO, UPS, INSA, Mines-Albi, 3 rue Caroline Aigle, 31400 Toulouse, France

## A B S T R A C T

### Keywords:

Nanoindentation  
Finite element modeling  
Inverse analysis  
Friction effect

The parameters describing the elastoplastic behavior of the 316 L austenitic stainless steel are identified through inverse analysis based on finite element modeling of the Berkovich nanoindentation test. The true geometry of the Berkovich indenter is introduced in axisymmetric and 3D finite element models using experimental nanoindentation data obtained by adapting the calibration method proposed by Oliver and Pharr [1]. Then, using these true indenter shape models, the elastoplastic parameters of the 316 L are estimated with high accuracy compared to the parameters obtained from tensile test identification. The indentation curve was correctly described by the numerical model for all the analyzed indentation depths, even for indentations inferior to 100 nm, which is a challenge until today. The 3D indenter model produces a residual imprint very close to the experimental indentation mark. The friction analysis between the indenter and the sample surface reveals small changes in the surface deformation, introducing an increase on the hardness, which disappears as the indentation depth decreases.

These studies demonstrate that the most important aspect in the elastoplastic parameter identification is the correct representation of the indenter geometry in the finite element model.

## 1. Introduction

Indentation is a popular method for evaluating elastic-plastic properties of materials and structures, including elastic modulus, hardness and yield strength [2,3]. Several research studies have used this test to analyze work-hardening, residual stress [4], and fracture toughness [5], etc., these properties are implicitly related with indentation response. This localized test can also be applied to measure the properties of individual phases as well as global properties of composite materials, coatings and multilayers [6,7]. Since it requires much less effort on sample preparation than other techniques, it is in particular useful for small material structures and biological materials (including living tissues). Due to the involved finite local deformation and nonlinear contact conditions, numerical modeling of indentation is a valuable tool to understand of the link between indentation data and material properties, and to correlate the indentation results with material parameters. Then, an inverse analysis can be carried out to identify these material properties from indentation tests.

The elastoplastic characterization of metals by nanoindentation test remains one of the biggest challenges in the micro-characterization domain [8,9,10]. The methods of elastoplastic characterization by nanoindentation test can provide access to the mechanical behavior [11] at multiple scales and in conditions where the conventional methods of mechanical characterization (e.g. tensile test) are difficult or impossi-

ble to apply, e.g. multi-layers systems, functionalized surfaces among others. The advantage of the use of the nanoindentation technique is that it is able to mechanically test volumes of matter in the microscale, producing experimental data of high accuracy.

The nanoindentation test produces two main pieces of information: the residual imprint and the loading-unloading curve (referred also as nanoindentation curve). The parameters describing the residual imprint and the nanoindentation curve are:  $h_m$  is the maximum displacement of the indenter measured from the free surface,  $h_c$  is the depth to the contact point;  $h_s$  is the distance from the contact point to the free surface,  $A(z)$  is the cross section area of the indenter at the contact point,  $P_m$  is the peak indentation load,  $S$  is the slope of the unloading branch of the nanoindentation curve, and  $h_f$  is the last point of contact between the indenter and the tested surface.

Actually, several methods of estimation of the elastic modulus and the hardness of the tested surface are available [12,13]. These methods purely elastic are based only on the unloading stage of the nanoindentation test (Fig. 1) [14]. In the case of the elastoplastic characterization, two main types of approaches have been developed since the apparition of the nanoindentation test: the analytical inverse methods [9,10,11] and the numerical inverse analysis [8,15].

In general terms, the analytical methods are based on the hypothesis of a representative strain associated with the geometry of the indenter [16], i.e. the strain induced in the surface is independent of the

\* Corresponding author.

E-mail address: [cmoises.sanchez@gmail.com](mailto:cmoises.sanchez@gmail.com) (C.-M. Sanchez-Camargo).

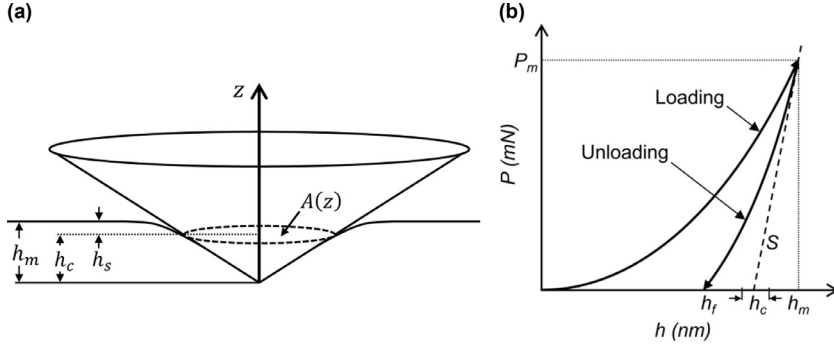


**Fig. 1.** (a) Schema of the indentation, and (b) typical corresponding nanoindentation curve.

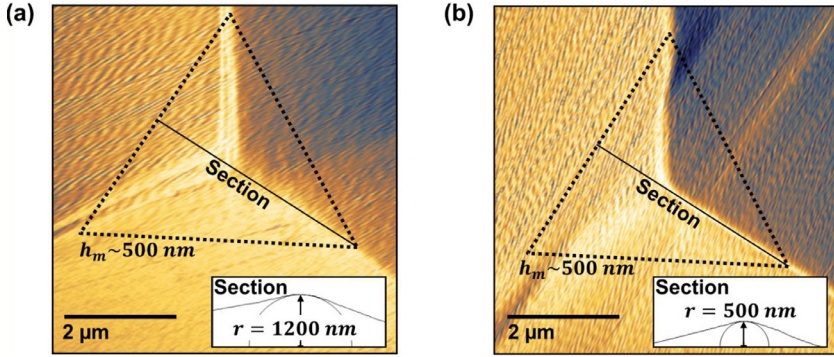


**Fig. 2.** Atomic Force Microscopy (AFM) captures of Berkovich indenters: (a) worn indenter with tip radius of 1200 nm and (b) new indenter with tip radius of 500 nm.

indentation depth. Using adimensional analysis [17], and finite element modeling, a vast amount of works has been published, for instance, among the most relevant, those presented in [18,19,20,21,22,47–50]. Such methods are based on finite element simulations of a wide range of elastoplastic parameters to determine the coefficients of the dimensionless functions. These methods were developed using the microindentation on a range of  $1 < h_m \leq 20 \mu\text{m}$ , where, according to the authors, the defects and deviations on the indenter can be neglected. In the nanoindentation scale, i.e.  $0 < h_m \leq 200 \text{ nm}$  [23,24], the wear and the deviations on the indenter tip are not negligible. The effects of these deviations on indenter shape are confirmed by Dao et al. [19], where they observed in finite element simulations that a variation of  $2^\circ$  on the half angle of a conical indenter results in 15 – 20% variations in the  $P - h$  loading curvature.

Since, in nanoindentation, the effects of the wear and deviations on the tip must be taken into account on finite element simulations a method to reproduce the physical indenter geometry in the finite element model is required. In general two approaches related to this issue can be found in the literature: i) the modeling of the indenter as a sphero-conical revolution shape [25,26,27,28,29] and ii) the modeling of the indenter from a cloud of points gathered with an atomic force microscope [30,31]. A remarkable example of the first approach was proposed by Pelletier et al. [25]. The principle of this method consists in the description of the Berkovich indenter based on the use of the function area proposed by Oliver et al. [1], which relates the cross section area of the indenter to the distance measured from its tip. From this function area an equivalent function area describing a sphero-conical indenter is derived. The limitation of this approach is that the indenter is sphero-conical; therefore the residual imprint cannot be compared with the experimental residual imprint of a Berkovich indenter.

The most relevant work found for the second approach was proposed by Krier et al. [30]. The authors captured the Berkovich indenter geometry with an Atomic Force Microscopy (AFM) and then introduce the true geometry in the finite element model. Their method is able to reproduce quite well indentations down to  $h_m = 40 \text{ nm}$ . However the implementation of the method is a challenge for several reasons, in particular the correction of the AFM cloud of points. In this work the

authors stated that the blunting tip defect affects the load-displacement curve, especially the loading phase, and also the elastic-plastic stress and strain fields beneath the indenter. They highlighted that this effect on the elastic-plastic strain field is a real and physical effect that cannot be avoided and limited by an analytical model [30]. This statement is verified through AFM captures of the two Berkovich indenters available for the present research (Fig. 2), which exhibit deviations on the selected operative range. But also the artefacts that must be corrected if the capture is used to reproduce the indenter geometry in the finite element model are visible.

Although the studies cited above address the problematic associated with the description of the physical Berkovich indenter, it does not exist, according to our present knowledge, a reliable and effective method to introduce the true indenter geometry on the finite element model allowing the correct representation of indentations on strain hardening solids in the interval  $0 < h_m \leq 500 \text{ nm}$ . The objective of this paper is to provide such method and evaluate the following aspects:

- 1 The ability of the proposed method to correctly describe the shape of the Berkovich indenter in both axisymmetric and 3D finite element models.
- 2 The accuracy of the elastoplastic parameters identification using the inverse analysis based on the finite element model including the true indenter geometry.
- 3 Numerical effects of the friction and its role in the nanoindentation simulation.

## 2. Experimental study

The material used in this research is the single-phase austenitic stainless steel AISI 316 L [32]. The microstructure is composed of equiaxed grains with a multitude of twinning (Fig. 3a). The grain size is between 10 and  $40 \mu\text{m}$ . The crystallographic structure of this austenitic phase is Face-Centered Cubic (FCC). The electron backscatter diffraction (EBSD) map shown in Fig. 3b highlights a non-textured material.

The mechanical behavior of the 316 L was characterized by uniaxial tensile test [33]. The Young's modulus obtained with this tensile test is  $E = 197 \text{ GPa}$ . The plastic deformation was fitted using a least squares

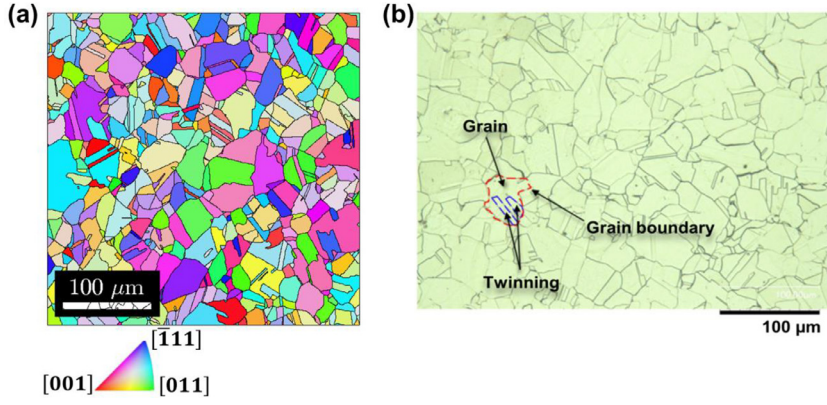


Fig. 3. (a) Microstructure and (b) texture of 316 L stainless steel.

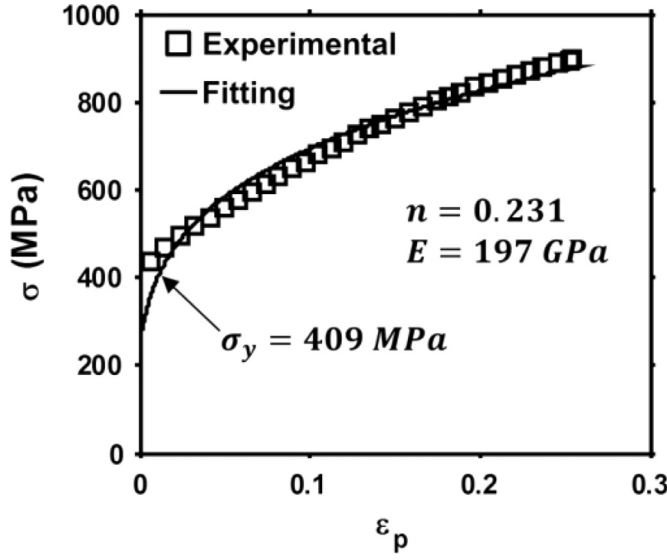


Fig. 4. True stress-true strain curve of 316 L stainless steel.

method (Fig. 4), according to the constitutive equation [19]:

$$\sigma = \sigma_y \left( 1 + \frac{E}{\sigma_y} \varepsilon_p \right)^n \quad (1)$$

where  $\sigma_y$  represents the yield stress and  $n$  the hardening exponent. The values of yield stress and hardening exponent identified from the tensile test, using an offset of 0.2 % plastic strain, were considered as the reference values of the elastoplastic parameters and were used as a comparison in the following to assess the accuracy of the analysis proposed in this paper:  $\sigma_y = 409 \text{ MPa}$  and  $n = 0.231$

### 2.1. Surface optimization for nanoindentation experiments

A nanoindentation specimen was machined in a cube of 2 cm side from the 316 L same round bar stock that was used for tensile test. In order to ensure a surface representative of the bulk material, the top layer of the machined surface was removed gradually following this iterative procedure: firstly, the initial height of the sample was measured. Then, mechanical grinding using SiC papers was down to 1200 grit and the final height has been re-determined again. Then, five nanoindentations using  $P_m = 50 \text{ mN}$  were conducted. Finally, the height of the pile-up from AFM captures of the residual imprint was estimated. Once the properties measured (i.e.  $h_m$  and pile-up) became consistent, the surface was polished using a diamond solution of  $1 \mu\text{m}$ , and finished with vibratory polishing using colloidal silica during eight hours with only sample weight [34]. The variations in the measures of  $h_m$  (Fig. 5(a)) and the height of the pile-up (Fig. 5(b)) during the procedure revealed that the machining process induced a gradient of properties, extending through a  $250 \mu\text{m}$  layer from the free surface of the sample.

The mean value of  $h_m$  was 820 nm on the stabilized surface, and 860 nm on the polished surface (Fig. 6(a)). The residual imprint on the polished surface revealed the influence of the crystallographic characteristics of the indented point in the form of asymmetric pile-ups (Fig. 6(b)).

The prepared surface was inspected by X-ray diffraction using  $\sin^2\psi$  method to analyze the residual stress state [35], finding  $\sigma_{11} = 12 \pm 8 \text{ MPa}$  and  $\sigma_{22} = -15 \pm 11 \text{ MPa}$ . The surface can thus be considered as free from internal stresses. The microstructural-crystallographic characteristics were determined through EBSD analysis. The treatment of the EBSD data [36] revealed a distortionless microstructure free of pre-hardening, with an intragranular misorientation ranging from  $0^\circ$  to  $4^\circ$  at the center of the grains (Fig. 7(a)). The roughness of the working surface was estimated from AFM captures (Fig. 7(b)); it was globally  $R_a = 4 \text{ nm}$  and locally  $R_a = 1.4 \text{ nm}$ . The local value of  $R_a$  was used to define the minimum valid value of  $h_m$  on this surface, which

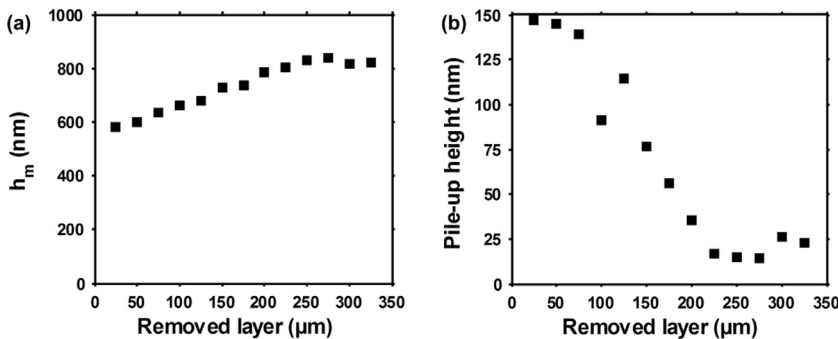
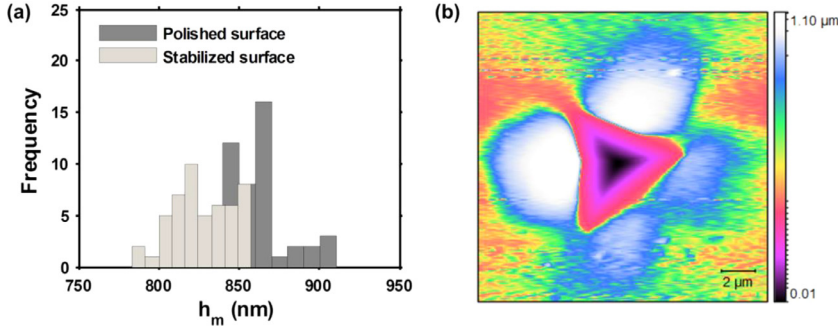
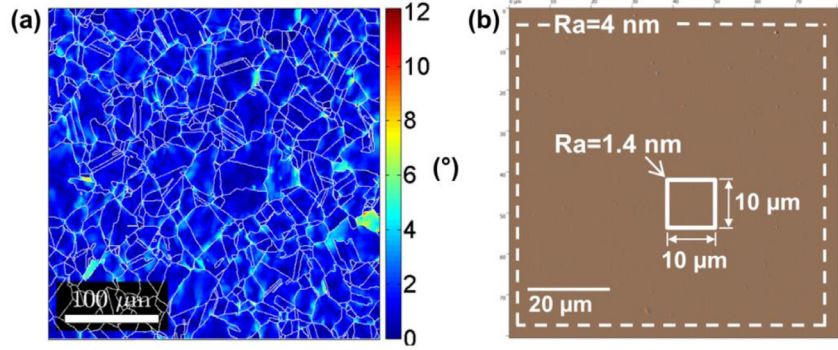


Fig. 5. Surface optimization procedure: (a) evolution of  $h_m$  and (b) evolution of the height of the pile-up as a function of the removed layer (affected by machining).





**Fig. 6.** Effects of polishing: (a) evolution of  $h_m$  and (b) residual imprint of the polished surface.



**Fig. 7.** Surface state of the polished surface: (a) crystallographic misorientation state and (b) roughness state.

**Table 1**  
Final surface properties.

Roughness	Crystallographic misorientation (pre-hardening)	Residual stresses
$R_a = 4 \text{ nm}$	less than $5^\circ$	$\sigma_{11} \approx 0 \text{ MPa} / \sigma_{22} \approx 0 \text{ MPa}$

is of about 28 nm, i.e. 20 times  $R_a$  [24]. The properties of the surface at the end of the preparation procedure are listed in Table 1.

## 2.2. Nanoindentation experiments

Once the working surface was prepared, the nanoindentation experiments were optimized and conducted on the polished surface. All the nanoindentation experiments were conducted using the worn Berkovich indenter of tip radius  $r = 1200 \text{ nm}$  (Fig. 2(a)) in load controlled mode at room temperature on a NHT2 commercial nanoindenter from Anton Paar instruments. The optimum loading/unloading rate was determined experimentally on the optimized working surface. Series of nanoindentation experiments were conducted using a constant loading force  $P_m = 10 \text{ mN}$  and varying the loading rate. The total indentation work ( $W_t$ , Eq. (11)) constant until a value of loading rate near to 25 mN/min, after this value,  $W_t$  increase linearly (Fig. 8(a)). Therefore we considered that using loading rates lower than 25 mN/min allows neglecting the time dependent effects (e.g. indentation creep) for  $P_m = 10 \text{ mN}$ .

On the smaller scale, the time dependent effects can be observed in the first stage of the loading nanoindentation curve ( $P_m$  between 0 and 0.5 mN), where loading rates greater than 6 mN/min introduce a slight increase in the loading curve (Fig. 8(b)). Finally using the loading rate close to 6 mN/min allows obtaining comparable indentation curves for different indentation loading values. The values of loading/unloading rate used in this study (Table 2) were selected respecting this rule, and considering the acquisition frequency to have similar quantity experimental points (i.e. using lower loading rates for the smaller  $P_m$ ).

Based on this information, the experimental protocol was defined (Table 2). This table also presents the  $h_m$  produced by the selected  $P_m$ .

**Table 2**  
Experimental protocol for indentation tests using the worn Berkovich indenter.

$P_m \text{ (mN)}$	$h_m \text{ (nm)}$	Loading/unloading rate (mN/min)
0.3	25	0.5
1	68	1
3	150	3
10	330	6
15	420	6

The maximum  $h_m$  is inferior to 500 nm, as required for the present study, and the minimum  $h_m$  is greater than 20 nm, which is valid with respect to the local roughness of the working surface (Fig. 7(b)).

A total of nine nanoindentations were applied for each of the five peak loads listed in the Table 2, spaced enough to avoid interferences. According to the literature [24], the indentation must be spaced at least three times the diameter of the imprint mark. In this study we used a spacing of ten times the diameter of the residual imprint. From each group of nine indentations the  $P - h$  curves sharing the same loading path were selected (Fig. 9(a)), and an AFM capture of their respective residual imprints was taken (Fig. 9(b)).

## 3. Numerical method

### 3.1. Finite element modeling of the specimen

All the simulations in this paper were conducted in controlled displacement applied to the indenter. The specimen was modeled as an axisymmetric body and as a full 3D model [37] using the implicit non-linear geometry FE algorithm in Abaqus [38].

Firstly, the axisymmetric model was optimized through a mesh refinement convergence analysis, using a fixed  $h_m = 500 \text{ nm}$ , a rigid cone equivalent to a perfect Berkovich indenter [39], a frictionless contact, and the elastoplastic parameters of the Eq. (1):  $E = 180 \text{ GPa}$ ,  $\sigma_y = 148 \text{ MPa}$ ,  $n = 0.278$  [40]. The iterative procedure was applied until the loading curve remained constant.

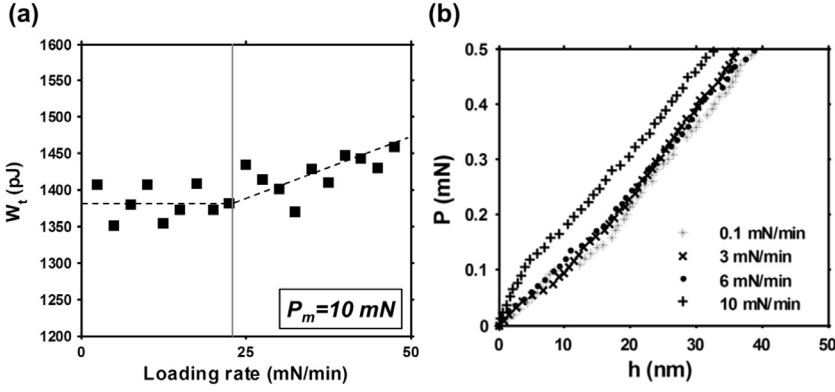


Fig. 8. Analysis of nanoindentation time dependent effects on 316L: (a) effects of loading rate on  $W_t$  and (b) effects of loading rate on the first portion of the loading nanoindentation curve.

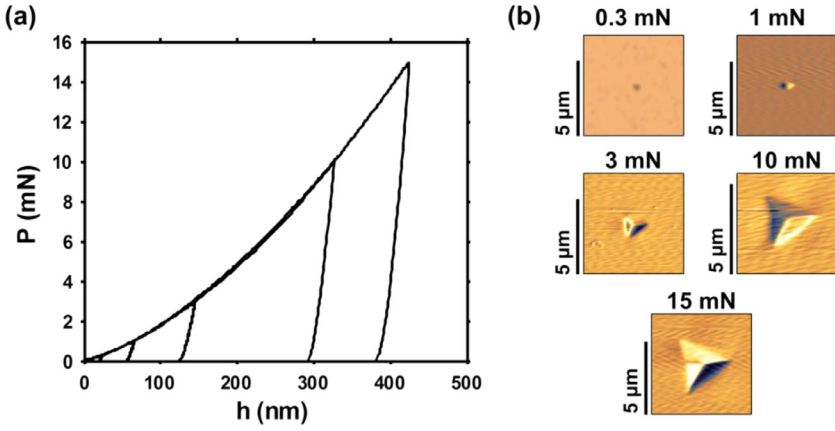


Fig. 9. Nanoindentation experiments using the worn Berkovich indenter: (a)  $P-h$  curves and (b) residual imprints associated to each  $P-h$  curve.

Once the optimum mesh and size of the specimen was found for the axisymmetric model (Fig. 10(a)), the characteristics of the axisymmetric model were replicated on the 3D model (Fig. 10(b)). Then, the mesh density of the 3D model was increased by adding partitions (Fig. 10(c)), until the loading curves of the 3D and the axisymmetric models were equivalents (Fig. 10(d)).

Finally both models were parametrized, using as master parameter  $h_m$ : therefore the same model was suitable for the analysis of a large range of  $h_m$ , ensuring similar contact conditions (Fig. 10(e)).

### 3.2. Finite element modeling of the indenter

The proposed method is based on the use of several values of the section area  $A$  of the indenter and their corresponding values of  $z$ , i.e.  $A(z)$ , with  $z$  the neutral axis of the indenter (Fig. 11). The values of  $A$  are used to define the points of the generatrix at the corresponding  $z$  values. Then, the generatrix is rotated around the  $z$  axis following a circular directrix to obtain a conical indenter (Fig. 11(a)). In the case of a 3D indenter, the generatrix is moved along a straight directrix to generate one wall of the indenter. Then, using a circular pattern the other three walls are generated and trimmed on the intersections (Fig. 11(b)). The steps required to obtain the generatrix for both indenters are explained below.

For simplicity, the explanation of the method is based on the assumption of a perfect Berkovich indenter (Fig. 11). Considering the area of the circular section of a cone, the associated radius is given by the equation:

$$r(z) = \sqrt{\frac{A(z)}{\pi}} \quad (2)$$

where  $r(z)$  is the generatrix in the axisymmetric finite element model (Fig. 11(a)).

Moving to the 3D indenter, the section of the indenter has a shape of an equilateral triangle (Fig. 11(b)). The length of each side of the

triangle is given by the equation:

$$a(z) = \sqrt{A(z) \frac{4}{\sqrt{3}}} \quad (3)$$

Then, the perpendicular distance from the axis of the indenter to the side of the triangle is computed from:

$$c(z) = \frac{a(z)}{2} \tan(30^\circ) \quad (4)$$

In this case  $c(z)$  is the generatrix of the wall, and  $a(z)$  is the directrix. Introducing the indenter on the finite element model requires the values of  $A$  along the axis  $z$  of the indenter. A well-known relation is the Berkovich function area  $A(z) = 24.5z^2$  [1]. Using this relation on the proposed procedure a perfect Berkovich indenter is generated, which is characterized by an angle  $\theta = 70.3^\circ$  in the case of an axisymmetric indenter (Fig. 11(a)), or by an angle  $\alpha = 65.3^\circ$  in the case of a 3D indenter (Fig. 11(b)).

Since the objective is to introduce the true indenter geometry on the finite element model, it is required to estimate  $A$  at several points of the  $z$  axis of the physical indenter. This problem was solved a few decades ago by Oliver and Pharr [1]. The principle of this method is to estimate  $A$  at a given contact depth,  $h_c$ , through the indentation on a well-known material (Fig. 1). On their work they proposed to use the fused quartz as indented material with the elastic constants  $E_s = 72 \text{ GPa}$  and  $\nu_s = 0.17$ ; and a diamond Berkovich indenter with the elastic constants  $E_i = 1141 \text{ GPa}$  and  $\nu_i = 0.07$ .

Firstly,  $A$  is calculated using the relation:

$$S = \frac{dP}{dh} = \frac{2}{\sqrt{\pi}} E_r \sqrt{A} \quad (5)$$

where  $S$  is the contact stiffness, computed at the initial portion of the unloading data (Fig. 1), and the reduced modulus,  $E_r$ , is computed using

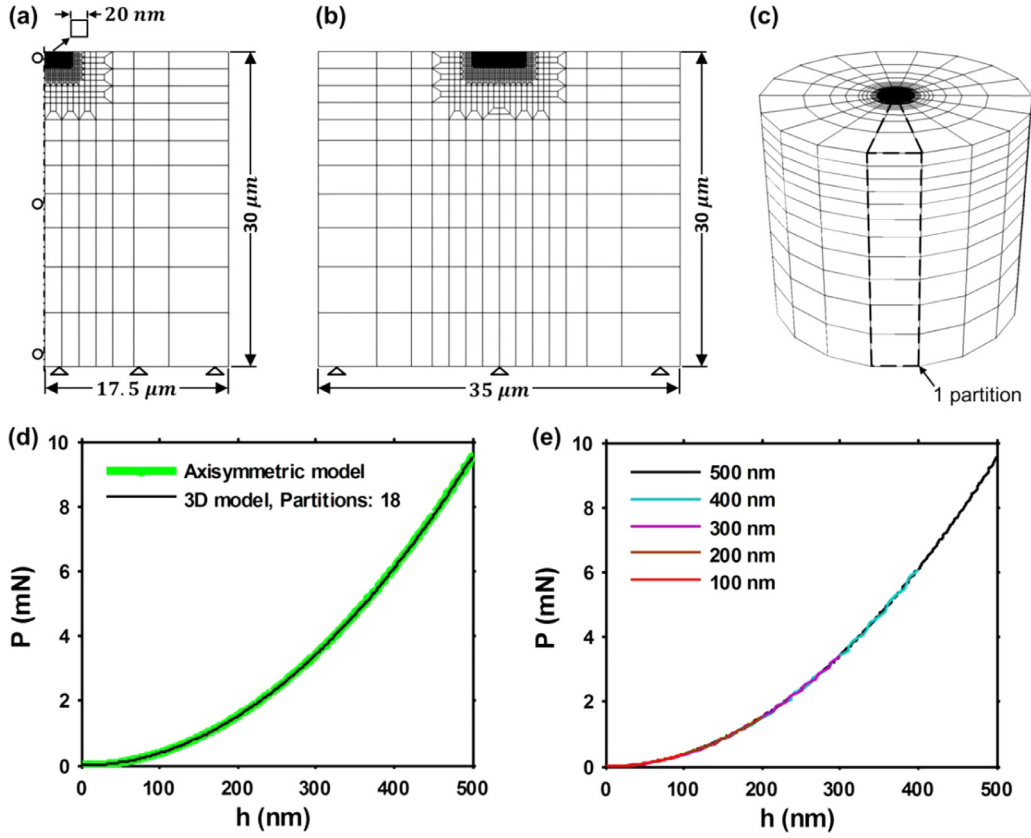


Fig. 10. Nanoindentation finite element modeling: (a) axisymmetric model (b) section of the 3D model (c) partitioning of the 3D model, (d) equivalence between the 3D and the axisymmetric model and (e) loading curves produced by the parametrized models on a wide range of  $h_m$ .

**Table 3**  
Experimental protocol for indentations on fused quartz.

	Indentation numbers	Peak load (mN)	Loading/unloading rate (mN/min)
Oliver and Pharr [1]	1–10	0.1	0.6
	11–20	0.3	1.8
	21–30	1	6
	31–40	3	18
	41–50	10	60
	51–60	20	120
Extension	61–70	40	240
	71–80	60	360
	81–90	80	480

the relation:

$$\frac{1}{E_r} = \frac{1 - \nu_s^2}{E_s} + \frac{1 - \nu_i^2}{E_i} \quad (6)$$

where  $\nu_s$  and  $E_s$  are the elastic constants for the specimen, and  $\nu_i$  and  $E_i$  are the same parameters for the indenter.

Then,  $h_c$  is computed from the equation:

$$h_c = h_m - h_s \quad (7)$$

where  $h_s$  is the deflection of the surface outside the contact area (Fig. 1), which is computed from the equation:

$$h_s = \frac{2}{\pi} (\pi - 2) \frac{P_m}{S} \quad (8)$$

On this study, the method of Oliver and Pharr [1] was used under three considerations: 1)  $h_c$  is equivalent to  $z$ , 2) the original nanoindentation protocol used on the fused quartz (Table 3), was extended to estimate the value of  $A$  for a corresponding value of  $z = 500$  nm, and

3) the elastic constants of the Berkovich indenter and the fused quartz were the same that those proposed by Oliver and Pharr [1]; both, the diamond Berkovich indenter and the standardized sample of fused quartz were obtained from the manufacturer of the *NHT2* nanoindenter. The indenters generated with the proposed procedure are referred as true indenters.

Finally, 9 values of  $A(z)$  were computed using the extended method of Oliver and Pharr [1] indenting on fused quartz (Fig. 12), to cover a maximum  $z = 500$  nm.

The physical Berkovich indenter was introduced in the finite element model applying this procedure through Python scripts in Abaqus, in separate models in the form of axisymmetric (Fig. 13(a)) and 3D (Fig. 13(b)) indenters, respectively. The experimental points  $A(z)$  were directly used to generate the indenter geometries adding an initial point in the origin. No fitting procedure was included to create the generatrix of the indenters. The axisymmetric model (Fig. 13(a)), is presented in the form of a cone using the visualization capabilities of Abaqus. The 3D indenter (Fig. 13(b)), is a full 3D representation of the physical Berkovich used in the experiments.

Once the characteristics of the specimen and the procedure to generate the indenter were established, the next step is to define the interaction behavior between the surfaces of the indenter and the specimen.

### 3.3. Indenter-specimen contact modeling

The interaction between the indenter and the specimen was defined in Abaqus Standard using the master-slave configuration [38]. The master surface was the external surface of the indenter, and the slave surface was the external top surface of the specimen. The interaction between the indenter and the specimen was analyzed in two ways: 1) in frictionless contact, and 2) with friction contact. The friction was introduced in the model using the formulation of Coulomb included in Abaqus



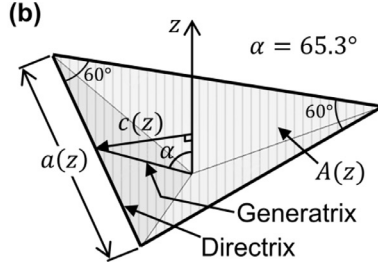
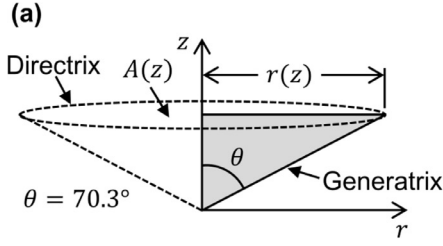


Fig. 11. Geometric specifications of the indenters: (a) conical indenter and (b) 3D indenter.

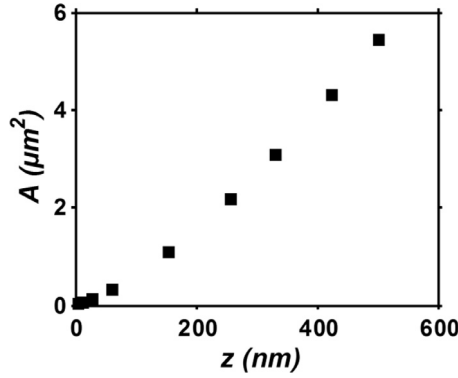


Fig. 12. Experimental points obtained from indentation on fused quartz using the worn Berkovich indenter.

[38]. This formulation assumes that there is no relative movement if the equivalent frictional stress given by

$$\tau_{eq} = \sqrt{\tau_1^2 + \tau_2^2} \quad (9)$$

is inferior to the critical stress,  $\tau_{crit}$ , which is proportional to the contact pressure,  $p$ , in the form:

$$\tau_{crit} = \mu p \quad (10)$$

The friction coefficient,  $\mu$ , is a function of the contact pressure,  $p$ , the slip rate, the average temperature, and the average field variables at the contact point. If  $\tau_{crit} = \tau_{eq}$ , slip occurs. In this study the friction is considered isotropic. The direction of the slip and the frictional stress is coincident.

### 3.4. Optimization procedure for elastoplastic parameters identification

The Levenberg-Marquardt [41] optimization algorithm was used to determine the elastoplastic behavior parameters. The objective function proposed is formulated using both loading and unloading branches of the  $P - h$  curve (Fig. 1).

From the loading curve the total indentation work,  $W_t$ , is obtained with the expression:

$$W_t = \int_0^{h_m} P dh \quad (11)$$

which is used to define the first component of the objective function in the form:

$$f_t = \frac{W_{tn} - W_{te}}{W_{te}} \quad (12)$$

where  $W_{tn}$  is the total indentation work obtained from the simulated loading curve, and  $W_{te}$  is the total indentation work obtained from the experimental loading curve.

Using the unloading curve, the elastic indentation work,  $W_e$ , is obtained through:

$$W_e = \int_{h_f}^{h_m} P dh \quad (13)$$

which is used to define the second component of the objective function in the form:

$$f_e = \frac{W_{en} - W_{ee}}{W_{ee}} \quad (14)$$

where  $W_{en}$  is the elastic indentation work obtained from the simulated unloading curve, and  $W_{ee}$  is the elastic indentation work obtained from the experimental unloading curve.

Using the Eqs. (12) and (14), the objective function for the whole  $P - h$  curve is assembled in the form:

$$f(\beta)_{min} = \begin{bmatrix} f_t \\ f_e \end{bmatrix} \quad (15)$$

where  $\beta$  represents the set of elastoplastic parameters. Finally, the minimization of the objective function is achieved using the algorithm shown in the Fig. 14.

The algorithm used in this work was set with a step tolerance and function tolerance of  $10^{-14}$ . Changes in residuals was set with a value of  $10^{-6}$ , and the number of iterations was set as infinite.

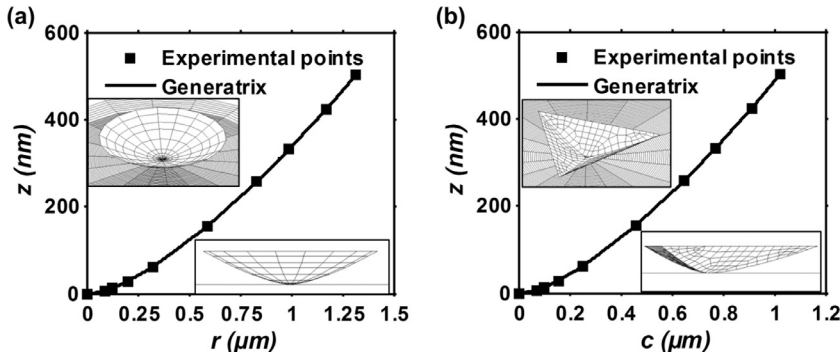


Fig. 13. Berkovich indenter modeling: (a) generatrix of the axisymmetric indenter and (b) generatrix of the 3D indenter.

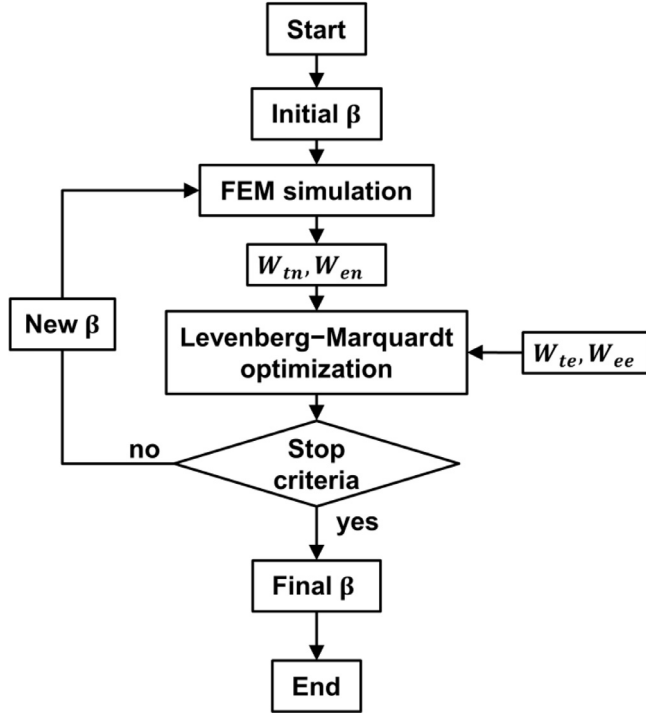


Fig. 14. Optimization algorithm used for the elastoplastic parameter estimation.

## 4. Results and discussion

### 4.1. The true indenter geometry modelling

For the investigated indenter height, i.e.  $0 \text{ nm} < z \leq 500 \text{ nm}$ , the profile of the true axisymmetric indenter (Fig. 15(a)), looks more like a parabola than a sphero-conical indenter as stated by some authors [25,26,27,28,29]. In fact, the profile of the true indenter never exhibits a parallelism with respect to the perfect indenter ( $70.3^\circ$ ). This found helps to explain why the polynomial form of the function area used by Oliver and Pharr [11] is able to describe the Berkovich indenter with high precision regardless a physical meaning. Another method to determine the function area, including a physical meaning, was proposed by Loubet et al. [42]. This method relies on the estimation of the height of a rounded portion (the tip defect), connected to a perfect indenter. The 3D indenter modeled with the method proposed in this paper cannot be de-

scribed using this assumption, because the sections of the true indenter are curved (Fig. 15(b)).

In addition, the cloud of points gathered by the Atomic Force Microscopy (AFM) was directly used for comparisons, founding that at least one of the three sections obtained from the AFM capture of the Berkovich tip is partially similar to the section of the true indenter, exhibiting a relation with the physical indenter.

### 4.2. Elastoplastic parameters identification

The three elastoplastic parameters of the 316 L constitutive model described in Eq. (1) were estimated from each experimental  $P-h$  curve obtained with the indentations using the worn Berkovich indenter (Fig. 9(a)) and the parameter identification routine (Fig. 14). Both perfect and true indenter models were used in the axisymmetric models, assuming frictionless contact ( $\mu = 0$  in Eq. (10)). The estimated parameters were plotted as a function of the maximum indentation depth in Fig. 16, and the values of the parameters obtained by tensile test were included as reference.

The three elastoplastic parameters obtained with the **perfect indenter model** increase with respect to the reference (tensile) value when  $h_m$  decreases. For the minimum value of  $h_m$ , the error in the hardening exponent reaches  $\%_{err} = 166$  i.e.  $n = 0.61$ , which is out of the range for metals [19]; the error in the yield stress reaches  $\%_{err} = 370$  and is also out of the parametric range of metals [19].

However, the elastic modulus and the hardening exponent estimated with the **true indenter model** exhibit a constant trend near the reference. The hardening exponent and the elastic modulus have a mean error  $\%_{err} = 3.7$  and  $\%_{err} = 17.8$  respectively compared to the reference. The error in the yield stress on the maximum value of  $h_m$  is  $\%_{err} = 21.6$ . This error increases with the decrease of  $h_m$  to reach  $\%_{err} = 72.9$ . In the literature, the increase of the yield strength with the decrease of  $h_m$ , reflected on the hardness, is referred as indentation size effect (ISE) [43,44,45]. We suppose that the ISE is already present in the maximum  $h_m$  investigated, and that is why the value of the elastic limit is greater than the value found by tensile test. This finding open the possibilities to new experimental-numerical studies of the ISE, besides the existing formulations based on the hardness e.g. the method of Gao et al. [44].

In addition, the parameter identification conducted with the perfect indenter model was close to the known (reference) solution for the indentation corresponding to the greater  $h_m$ . This effect can be easily observed in the  $P-h$  curves, where the simulation of the shallow indentation exhibits a great difference with respect to the experimental curve (Fig. 17(a)), while in the deepest indentation the difference between them is reduced (Fig. 17(b)). Nevertheless, the parameter estimation performed using the true indenter geometry showed powerful

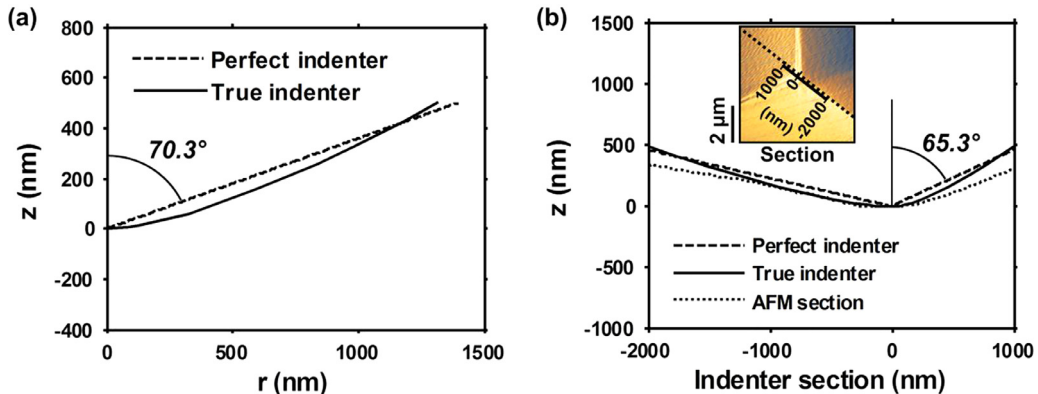


Fig. 15. Comparison between the profiles of perfect indenters and the true indenters: (a) axisymmetric indenter and (b) 3D indenter.

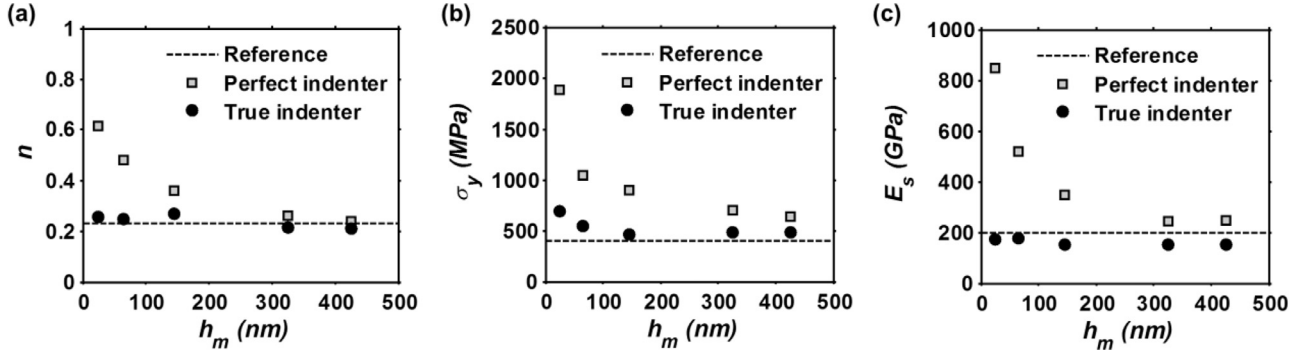


Fig. 16. Elastoplastic parameters evolution in function of  $h_m$ .

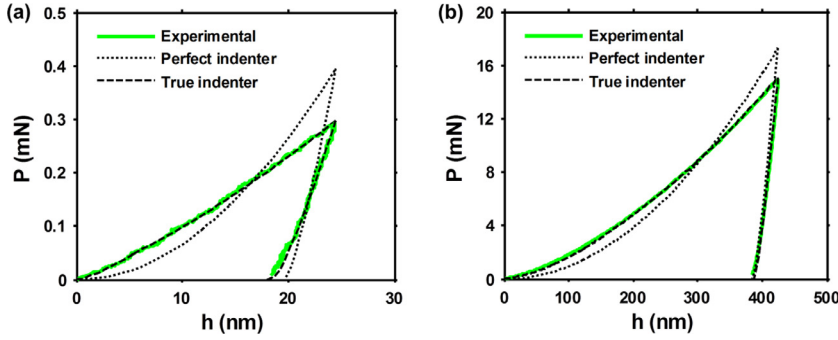


Fig. 17. Comparison between the true indenter and the perfect indenter  $P-h$  curves in (a) shallow and (b) deep indentations.

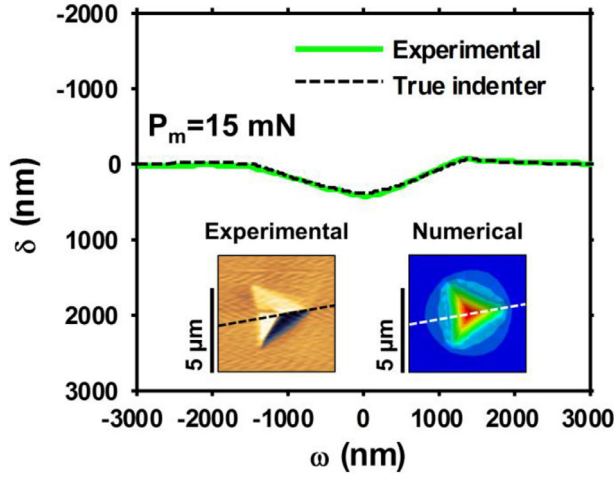


Fig. 18. Comparison between the experimental residual imprint profile and the numerical residual imprint profile obtained with the 3D model.

capabilities of this model to faithfully reproduce the experimental curve for deep and shallow indentations (Fig. 17(a) and (b)).

Finally, the section of the residual imprint produced by the 3D true indenter model with  $P_m = 15$  mN, for the respective determined elastoplastic parameters, is very close at least to one of the three sections obtained experimentally (Fig. 18). This great resemblance also confirms that the optimization routine converged to the correct solution in this case.

#### 4.3. Friction analysis

The parameter identification routine was executed two times separately using the friction coefficients  $\mu = 0.1$  and  $\mu = 0.2$  respectively, for each investigated experimental indentation on the 316 L. The starting point of the routine was the last set of parameters determined with

the frictionless configuration of each parameter identification execution. The true indenter finite element model was used. In all cases, after a few iterations the routine stopped because the changes in the curve were negligible (Fig. 19(a) and (b)), in consequence the changes in the value of the parameters were also negligible. Therefore, the effect of the investigated friction coefficients ( $\mu = 0$ ;  $\mu = 0.1$ ;  $\mu = 0.2$ ) were evaluated using the determined elastoplastic parameters for the experimental  $P_m = 15$  mN. The residual imprint showed a decrease of the height of the pile-up (until 31 nm for  $\mu = 0.2$ ), compared to the frictionless contact (Fig. 19(c)), revealing small variations in the contact area.

Based on this evidence, the hardness,  $H = P_m/A(h_c)$  [1], was computed for the experimental  $P-h$  curves with  $P_m = 3$  mN,  $P_m = 10$  mN and  $P_m = 15$  mN using the AFM captures of their corresponding residual imprints. In the case of the numerical models,  $A(h_c)$  was determined at  $h_m$ . The results were plotted in function of  $h_m$  (Fig. 20). The results show an increase of  $H$  with the decrease of  $h_m$ . For the indentations inferior to  $h_m = 200$  nm, the effects of the friction are reduced, i.e. the changes in the contact area are negligible. For indentations superior to  $h_m = 200$  nm, the experimental  $H$  is close to the simulation using frictionless contact, and the increase when  $\mu = 0.2$  induces  $\%_{err} = 19.6$ , meaning a difference of  $H$  about 490 MPa.

The literature reports a maximum increase of  $\sim 20\%$  in the hardness for contacts with friction coefficients  $\mu > 0$  [46]. The maximum difference found in this work ( $\%_{err} = 19.6$ ) is consistent with these observations. However, for the deeper indentations analyzed in this work, the values of the hardness obtained using frictionless contact are closer to the experimental values.

Mata et al. [46] observed two effects of the friction on the pile-up: 1) the height of the pile-up decreases with the increase of the friction coefficient, and 2) the indentations with low height of pile-up are less sensitive to the variations of the friction coefficient. The two effects observed by Mata et al. are presented in this study (Fig. 21). The first one is observed with indentations of  $h_m > 300$  nm, where a maximum difference of 27.8 nm on the height of the pile-up is observed comparing frictionless contact and contact with friction coefficient  $\mu = 0.2$ . The second effect is observed with indentations of  $h_m < 100$  nm, where the height of the pile-up is similar regardless the value of  $\mu$ .

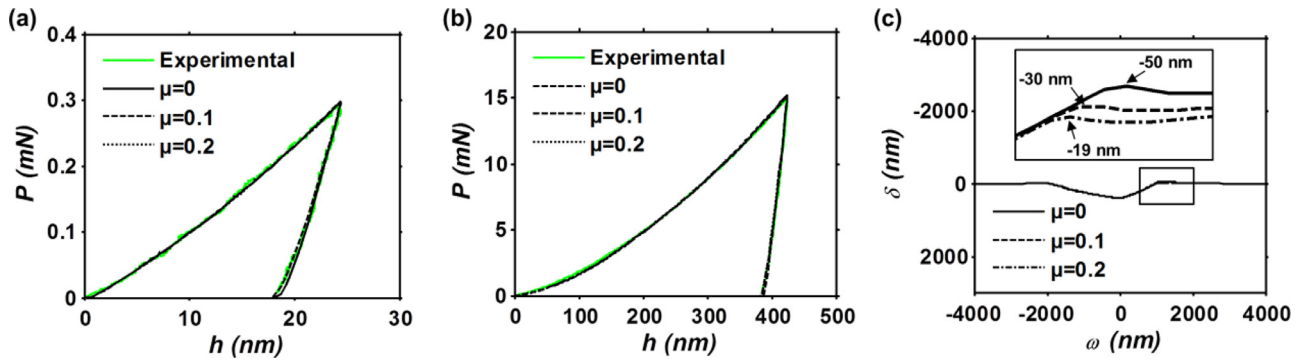


Fig. 19. Friction effects: (a) in shallow and (b) in deep indentation, on the  $P - h$  curves, (c) on the residual imprint.

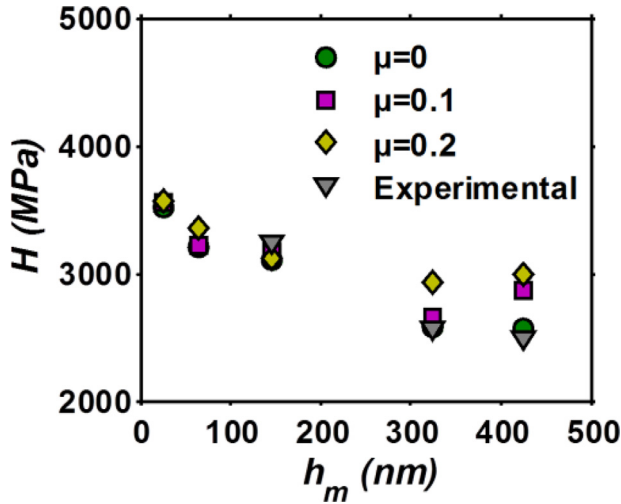


Fig. 20. Friction coefficient effect on the surface hardness.

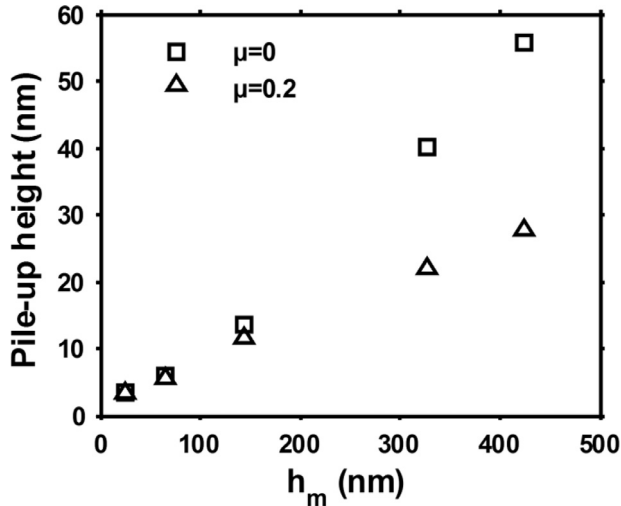


Fig. 21. Effects of the variations of the friction coefficient on the pile-up height.

## 5. Conclusion

A new methodology to improve the representation of the geometry of the physical Berkovich indenter in the finite element model is proposed in this paper.

This inclusion of the physical indenter in the finite element model leads to a correct reproduction of the experimental  $P - h$  curve and

residual imprint of the tested material, providing an estimation of the elastoplastic parameters with significantly improved accuracy in the operative range  $0 < h_m \leq 500$  nm. The observed variations of the yield stress as a function of the indentation depth open new insights on the indentation size effect, which now can be analyzed through sophisticated numerical models on indentations with  $h_m < 100$  nm. This paper focused on the analysis of strain hardening solids, however complex micromechanical systems (e.g. ultrathin layers, nanocrystalline structures, etc.) can be analyzed using the accurate finite element model of the indenter geometry.

The effects of the friction coefficient were observed in the contact interface between the indenter and the sample surface modifying the value of the hardness, which is in good agreement with other works reported in the literature. No effects of the friction coefficient used in the finite element simulations were observed on the  $P - h$  curve or on the estimated parameters.

## Declaration of Competing Interest

None.

## Acknowledgments

This work was partially supported by the Mexican Council of Science and Technology (CONACYT). The assistance of Dr. Victor Sanchez in the review of this manuscript is gratefully acknowledged. We wish to acknowledge the assistance of Mr. Thierry Martin for the optimum performance of the nanoindenter, and the support of all the ISAE-SUPAERO DMSM team.

## References

- [1] Oliver WC, Pharr GM. An improved technique for determining hardness and elastic modulus using load and displacement sensing indentation experiments. *J Mater Res* 1992;7:1564–83.
- [2] Iracheta O, Bennett C, Sun W. Characterization of material property variation across an inertia friction welded CrMoV steel component using the inverse analysis of nanoindentation data. *Int J Mech Sci* 2016;107:253–63.
- [3] Ben Ismail A, Rachik M, Mazeran P-E, Fafard M, Hug E. Material characterization of blanked parts in the vicinity of the cut edge using nanoindentation technique and inverse analysis. *Int J Mech Sci* 2009;51:899–906.
- [4] Zhu L, Xu B, Wang H, Wang C. Measurement of residual stress in quenched 1045 steel by the nanoindentation method. *Mater Charact* 2010;61(12):1359–62.
- [5] Romana L, Thomas P, Bilas P, Mansot JL, Aldana Aranda D. Use of nanoindentation technique for a better understanding of the fracture toughness of *Strombus gigas* conch shell. *Mater Charact* 2013;76:55–68.
- [6] Lai D, Xu J, Xie Z, Habibi D, Munroe P. Mechanical characterization of a novel nanocrystalline coating: first-principles calculations and nanoindentation. *Mater Charact* 2012;68:1–6.
- [7] Bouzakis K-D, Michailidis N, Hadjiyiannis S, Skordaris G, Erkens G. The effect of specimen roughness and indenter tip geometry on the determination accuracy of thin hard coatings stress-strain laws by nanoindentation. *Mater Charact* 2002;49(2):149–56.
- [8] Kang J, Becker A, Sun W. Determining elastic-plastic properties from indentation data obtained from finite element simulations and experimental results. *Int J Mech Sci* 2012;62:34–46.

- [9] Kim M, Pandian Marimuthu K, Lee JH, Lee H. Spherical indentation method to evaluate material properties of high-strength materials. *Int J Mech Sci* 2016;106:117–27.
- [10] Nguyen N-V, Kim JJ, Kim S-E. Methodology to extract constitutive equation at a strain rate level from indentation curves. *Int J Mech Sci* 2019;152:363–77.
- [11] Pham T-H, Kim JJ, Kim S-E. Estimating constitutive equation of structural steel using indentation. *Int J Mech Sci* 2015;90:151–61.
- [12] Oliver WC, Pharr GM. An improved technique for determining hardness and elastic modulus using load and displacement sensing indentation experiments. *J Mater Res* 1992;7(6):1564–83.
- [13] Oliver WC, Pharr GM. Measurement of hardness and elastic modulus by instrumented indentation: advances in understanding and refinements to methodology. *J Mater Res* 2004;587(1):3–20.
- [14] Bulychiev S, Alekhin V, Shorshorov MK, Ternovskii A. Mechanical properties of materials studied from kinetic diagrams of load versus depth of impression during microimpression. *Strength Mater* 1976;8(9):1084–9.
- [15] Kang JJ, Becker AA, Wen W, Sun W. Extracting elastic-plastic properties from experimental loading-unloading indentation curves using different optimization techniques. *Int J Mech Sci* 2018;144:102–9.
- [16] Tabor D. The hardness of solids. *Review of Physics in Technology* 1970;1(3):1–145.
- [17] Barenblatt GL. Scaling, self-similarity, and intermediate asymptotics: dimensional analysis and intermediate asymptotics. Cambridge University Press; 1996.
- [18] Cheng Y-T, Cheng C-M. Scaling approach to conical indentation in elastic-plastic solids with work hardening. *J Appl Phys* 1998;84(3):1284–91.
- [19] Dao M, v Chollacoop N, Van Vliet KJ, Venkatesh TA, Suresh S. Computational modeling of the forward and reverse problems in instrumented sharp indentation. *Acta Mater* 2001;49:3899–918.
- [20] Buaillle J-L, Stauss S, Felder E, Michler J. Determination of plastic properties of metals by instrumented indentation using different sharp indenters. *Acta Mater* 2003;51:1663–78.
- [21] Chollacoop N, Dao M, Suresh S. Depth-sensing instrumented indentation with dual sharp indenters. *Acta Mater* 2003;51(13):3713–29.
- [22] Ogasawara N, Chiba N, Chen X. Measuring the plastic properties of bulk materials by single indentation test. *Scr Mater* 2006;54:65–70.
- [23] ISO 14577-1:2015. Metallic materials - Instrumented indentation test for hardness and materials parameters, part 1: test method. Switzerland: Geneve; 2002.
- [24] Fischer-Cripps AC. Nanoindentation testing. Springer; 2011. p. 21–37.
- [25] Pelletier H, Krier J, Cornet A, Mille P. Limits of using bilinear stress-strain curve for finite element modeling of nanoindentation response on bulk materials. *Thin Solid Films* 2000;379:147–55.
- [26] Bouzakis K-D, Pappa M, Maliaris G, Michailidis N. Fast determination of parameters describing manufacturing imperfections and operation wear of nanoindenter tips. *Surf Coat Technol* 2013;215:218–23.
- [27] Berla LA, Allen AM, Han SM, Nix WD. A physically based model for indenter tip shape calibration for nanoindentation. *J Mater Res* 2010;25(4):735–45.
- [28] Yu N, Polycarpou AA, Conry TF. Tip-radius effect in finite element modeling of sub-50 nm shallow nanoindentation. *Thin Solid Films* 2004;450(2):295–303.
- [29] Chen W, Li M, Zhang T, Cheng Y-T, Cheng C-M. Influence of indenter tip roundness on hardness behavior in nanoindentation. *Mater Sci Eng* 2007;445:323–7.
- [30] Krier J, Breuils J, Jacomine L, Pelletier H. Introduction of the real tip defect of Berkovich indenter to reproduce with FEM nanoindentation test at shallow penetration depth. *J Mater Res* 2012;27(1):28–38.
- [31] Herrmann K, Hasche K, Pohlenz F, Seemann R. Characterisation of the geometry of indenters used for the micro-and nanoindentation method. *Measurement* 2001;29(3):201–7.
- [32] Sapezanskaia I, Roa JJ, Fargas G, Turon-Viñas M, Mateo A. Deformation mechanisms induced by nanoindentation tests on a metastable austenitic stainless steel: a FIB/SIM investigation. *Mater Charact* 2017;131:253–60.
- [33] Davis JR. Tensile testing. ASM International; 2004.
- [34] Wang Z, Bei H, George EP, Pharr GM. Influences of surface preparation on nanoindentation pop-in in single-crystal Mo. *Scr Mater* 2011;65(6):469–72.
- [35] Basrour S, Robert L. X-ray characterization of residual stresses in electroplated nickel. *Mater Sci Eng* 2000;288(2):270–4.
- [36] Bachmann F, Hielscher R, Schaeben H. Texture analysis with MTEX - free and open source software toolbox. *Solid State Phenom* 2010;160:63–8.
- [37] Larsson P-L. Investigation of sharp contact at rigid-plastic conditions. *Int J Mech Sci* 2001;43:895–920.
- [38] M. Smith, ABAQUS/Standard User's Manual, Version 6.9, Simulia, 2009.
- [39] Bolshakov A, Pharr GM. Influences of pileup on the measurement of mechanical properties by load and depth sensing indentation techniques. *J Mater Res* 1998;13:1049–58.
- [40] Beghini M, Bertini L, Fontanari V. Evaluation of the stress-strain curve of metallic materials by spherical indentation. *Int J Solids Struct* 2006;43:2441–59.
- [41] Marquardt DW. An algorithm for least-squares estimation of nonlinear parameters. *J Soc Ind Appl Math* 1963;11(2):431–41.
- [42] Loubet JL, Georges JM, Marchesini O, Meille G. Vickers indentation curves of magnesium oxide (MgO). *J Tribol* 1984;106:43–8.
- [43] Swadener J, George E, Pharr G. The correlation of the indentation size effect measured with indenters of various shapes. *J Mech Phys Solids* 2002;50(4):681–94.
- [44] Nix WD, Gao H. Indentation size effects in crystalline materials: a law for strain gradient plasticity. *J Mech Phys Solids* 1998;46:411–25.
- [45] Shim S, Bei H, George EP, Pharr GM. A different type of indentation size effect. *Scr Mater* 2008;59(10):1095–8.
- [46] Mata M, Alcalá J. The role of friction on sharp indentation. *J Mech Phys Solids* 2004;52(1):145–65.
- [47] Cao YP, Lu J. A new method to extract the plastic properties of metal materials from an instrumented spherical indentation loading curve. *Acta Mater* 2004;52:4023–32.
- [48] Casals O, Alcalá J. The duality in mechanical property extractions from Vickers and Berkovich instrumented indentation experiments. *Acta Mater* 2005;53:3545–61.
- [49] Gao X-L, Jing XN, Subhash G. Two new expanding cavity models for indentation deformations of elastic strain-hardening materials. *Int J Solids Struct* 2006;43:2193–208.
- [50] Giannakopoulos AE, Suresh S. Determination of elastoplastic properties by instrumented sharp indentation. *Scr Mater* 1999;40:1191–8.